



Aalborg Universitet

AALBORG UNIVERSITY  
DENMARK

## New Inter- and Inner-Phase Power Control Method for Cascaded H-Bridge Based on Simplified PWM Strategy

Ye, Zongbin; Zheng, Qisheng; Pei, Hanjun; Guerrero, Josep M.; Mao, Shiqi; Wang, Tingting; Chen, Anni; Zhang, Zhiguo; Jiang, Linlin; Yu, Dongsheng; Fernando, Tyrone

*Published in:*  
IEEE Transactions on Power Electronics

*DOI (link to publication from Publisher):*  
[10.1109/TPEL.2019.2961945](https://doi.org/10.1109/TPEL.2019.2961945)

*Publication date:*  
2020

*Document Version*  
Accepted author manuscript, peer reviewed version

[Link to publication from Aalborg University](#)

*Citation for published version (APA):*  
Ye, Z., Zheng, Q., Pei, H., Guerrero, J. M., Mao, S., Wang, T., Chen, A., Zhang, Z., Jiang, L., Yu, D., & Fernando, T. (2020). New Inter- and Inner-Phase Power Control Method for Cascaded H-Bridge Based on Simplified PWM Strategy. *IEEE Transactions on Power Electronics*, 35(8), 8607-8623. [8941294]. <https://doi.org/10.1109/TPEL.2019.2961945>

### General rights

Copyright and moral rights for the publications made accessible in the public portal are retained by the authors and/or other copyright owners and it is a condition of accessing publications that users recognise and abide by the legal requirements associated with these rights.

- Users may download and print one copy of any publication from the public portal for the purpose of private study or research.
- You may not further distribute the material or use it for any profit-making activity or commercial gain
- You may freely distribute the URL identifying the publication in the public portal -

### Take down policy

If you believe that this document breaches copyright please contact us at [vbn@aub.aau.dk](mailto:vbn@aub.aau.dk) providing details, and we will remove access to the work immediately and investigate your claim.

# New Inter and Inner Phase Power Control Method for Cascaded H-Bridge Based on Simplified PWM Strategy

Zongbin Ye, *Member, IEEE*, Qisheng Zheng, Hanjun Pei, Josep M. Guerrero, *Fellow, IEEE*, Shiqi Mao, Tingting Wang, Anni Chen, Zhiguo Zhang, Linlin Jiang, Dongsheng Yu, *Member, IEEE*, and Tyrone Fernando, *Senior Member, IEEE*

**Abstract-** Cascaded H-Bridge (CHB) converters characterized with high scalability have been widely used in photovoltaic (PV) and energy storage systems. However, the three-phase power and the voltages are often unequal due to various reasons, making the system less efficient. Therefore, the ability to deal with unequal power is necessarily required in CHB. This paper proposes three inter-phase power control methods based on simplified PWM strategy to improve the efficiency of the system. A control method with better performance both in dynamic and steady states is adopted to adjust power distribution. The relationship between duration times and DC power is analyzed. On the basis of controlling the inter-phase power, an inner-phase power control method is proposed by redistributing the duration time of each submodule, to further enhance the power control ability of the system. The simulation and experimental results show that under the condition of balanced or unbalanced voltage, the inter-phase and inner-phase power can be controlled, which verifies the feasibility and practicability of several modulation strategies proposed in this paper.

**Keywords-** pulse width modulation, multilevel systems, DC-AC power conversion, power control.

## I. INTRODUCTION

Renewable energy sources such as wind and solar energy have attracted wide research attention, as the low-carbon economy is globally advocated. Photovoltaic (PV) power systems can realize clean electricity generation and hence

reduce the dependence on fossil fuels [1]. For large photovoltaic generation systems, Cascaded H-Bridge (CHB) is regarded as one of the prime candidates for the lasted megawatt-class PV converters [2]-[4]. Compared with other topologies, CHB can provide smoother output voltage, better scalability and low voltage stress on switches [5]-[8].

Despite the fact that CHB structure can achieve higher conversion efficiency and can be easily extended to more levels [9], it is confronted with the problem that the power generated by PV modules is often unbalanced [10]. This can be attributed to non-uniform solar irradiance, unequal temperature, inconsistent module degradation and other factors [11], [12]. Similar problems also exist in the field of energy storage systems. In microgrid, SoC of energy storage systems is always unbalanced due to the difference in line impedances and the initial value of SoC [13]. Differences of SoC in energy storage systems will cause uneven power generation. Power imbalance, including inter phase power imbalance and inner phase power imbalance, will further result in the imbalance in three-phase currents, which, as delivered to the grid, may lead to the PV generation system disconnect from the grid [14].

To address this problem, several control strategies have been proposed. Injecting zero-sequence voltage can help to reduce DC power imbalance [15]. To simplify the computation, a novel weighting min-max zero-sequence voltage injection method is proposed in [16] and applied to grid-connected PV systems [17]. The zero sequence voltage in this method, is equal to half of the sum of the maximum and minimum values, wherein the maximum and minimum values are obtained from the product of the power imbalance ratio and the corresponding voltage reference. Although this method can achieve power balance, it does not analyze the controllable range of power. In [10]-[12], an optimal zero sequence voltage injection method is proposed and applied to PV topologies. In this way, the problem of inter-phase power imbalance can be solved. However, the DC power in this method always deviates from the expected values because it equals the power on the grid side to the power on the converter side during the derivation process, making the power control inaccurate. Besides, the relationship between the linear modulation index and power generation ratios limitation, which is important for PV systems under different

---

This work was supported by the Fundamental Research Funds for the Central Universities under Award 2019XKQYMS36.

Z. Ye, Q. Zheng, H. Pei, S. Mao, T. Wang, and D. Yu are with the School of Electrical and Power Engineering, China University of Mining and Technology, Xuzhou 221008, China (e-mail: yezongbin@163.com; w1373529836@163.com; 18772289282@163.com; 17851147002@163.com; wangtt\_1994@163.com; dongsiee@163.com).

J. M. Guerrero is with the Department of Energy Technology, Aalborg University, 9220 Aalborg East, Denmark. (Tel: +45 2037 8262; Fax: +45 9815 1411; e-mail: joz@et.aau.dk).

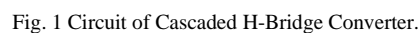
A. Chen is with the Zhongtian Construction Group Co., Ltd., Hangzhou 310020, Zhejiang, China (e-mail: anne1993chen@163.com).

Z. Zhang is with the State Grid Yantai Power Supply Company, Yantai 264000, Shandong, China (e-mail: zgwangyinet@163.com).

L. Jiang is with the State Grid Jiaxing Power Supply Company, Jiaxing 314000, Zhejiang, China (e-mail: jianglinlin0410@163.com).

T. Fernando is with the School of Electrical, Electronic and Computer Engineering, University of Western Australia, Crawley, WA 6009, Australia (e-mail: tyrone.fernando@uwa.edu.au).

This paper proposes three inter-phase power control methods based on simplified PWM modulation strategy [20] to achieve precise DC power control. In these methods, each phase or submodule is properly set to operate at different output power to improve the efficiency of the system and help achieving MPPT [17], [21]. Balanced three-phase currents can



The rest of this paper are organized as follows. Section II introduces the simplified PWM strategy and the DC power calculation. Then, three inter-phase power control methods are derived in Section III and an inner-phase power control method is derived in Section IV. Section V analyzes the control limitation of power control. The simulations and experiments of a three-phase five-level CHB converter are conducted in Section VI. In Section VII, the final conclusions are drawn.

$$T_X' = \left[ \frac{u_{X\text{ref}} T_s}{U_{dc}} + \frac{1 - \text{sgn}(u_{X\text{ref}})}{2} \cdot n T_s \right] - \Delta T = T_X - \Delta T \quad (2)$$

The relationship between the duration time of each phase and the duration times of submodules can be expressed by (3), where  $T_{Xi}$  is the duration time of corresponding submodule.

$$T_X = T_{X_1} + T_{X_2} + \dots + T_{X_n} \quad (3)$$

The  $\Delta T$  in (2) represents the correction value of  $T_X$ , and it can be used to achieve such targets as minimum pulse width compensation, switching losses reduction [22], linear modulation index extension [23]. And  $\Delta T$  can also be used to achieve DC-power control with good performance and convenience [20]. However, it should be noted that the three effects, minimum pulse width compensation, switching losses reduction and active power control, cannot be achieved in the meantime, since the pulse distribution methods of them are different. To realize the linear modulation,  $\Delta T$  should satisfy (4), and the existent condition of  $\Delta T$  can be expressed by inequality (5).

$$0 \leq T_X' = T_X - \Delta T \leq nT_s \quad (4)$$

$$\underbrace{\max(T_A, T_B, T_C) - nT_s}_{\Delta T_{\min}} \leq \Delta T \leq \underbrace{\min(T_A, T_B, T_C)}_{\Delta T_{\max}} \quad (5)$$

### B. DC power analysis and calculation

In order to get higher control precision of DC power, this paper employs a method based on the calculation of one carrier-wave period DC power.

#### 1) The principle of computing DC power

Ignoring converter losses, the power calculated in the DC side is equal to the AC side. As the system is stable, the DC power per submodule in a fundamental period can be given by (6),

$$\begin{cases} P_{A_i} = \frac{1}{T} \int_t^{t+T} U_{dc\_A_i} \cdot i_{dc\_A_i} dt \\ P_{B_i} = \frac{1}{T} \int_t^{t+T} U_{dc\_B_i} \cdot i_{dc\_B_i} dt \\ P_{C_i} = \frac{1}{T} \int_t^{t+T} U_{dc\_C_i} \cdot i_{dc\_C_i} dt \end{cases} \quad (6)$$

where  $i_{dc\_Xi}$  is the DC side current,  $U_{dc\_Xi}$  is the DC side voltage,  $i_X$  is the phase current, and  $S_{Xi}$  is the switching function of each submodule, satisfying  $S_{Xi} = S_{Xi1} - S_{Xi2}$ , and  $T$  is the fundamental period.

$$i_{dc\_X_i} = i_X \cdot S_{X_i} \quad (7)$$

Combining (6) with (7), introducing (8)

$$P_{X_i} = \frac{1}{T} \int_t^{t+T} U_{dc\_X_i} \cdot i_X \cdot S_{X_i} dt \quad (8)$$

Since the sampling frequency is high, the DC side voltages and currents ( $U_{dc\_Xi}$ ,  $i_{dc\_Xi}$ ) remain constant, then (6) can be rewritten as (9),

$$P_{X_i} = \frac{1}{N} \sum_{k=0}^N p_{X_i}(k) \quad (9)$$

where

$$p_{X_i}(k) = U_{dc\_X_i}(k) i_X(k) \cdot [T_X(k) - \frac{1 - \text{sgn}(u_{\text{Xref}}(k))}{2} \cdot nT_s - \Delta T(k)] \cdot \frac{1}{T_s} \quad (10)$$

$$N = \text{floor}(T/T_s) \quad (11)$$

Where  $T$  represents the fundamental period, and  $T_s$  represents the carrier-wave period.

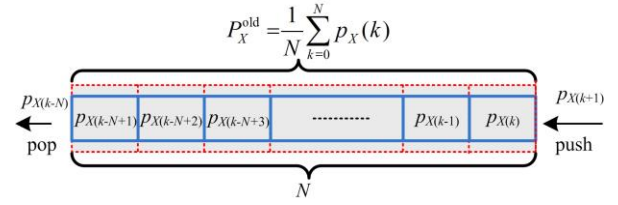


Fig. 2 Diagram of FIFO.

Equation (10) expresses the DC power generated by submodule  $i$  of phase  $X$  within  $T_s$ . Thus the DC power generated by one phase within one fundamental period can be expressed by (12).

$$P_X = \sum_{i=1}^n P_{X_i} \quad (12)$$

By combining (9), (10) and (12), the DC power generated by one phase can be rewritten as (13),

$$P_X = \frac{1}{N} \sum_{k=0}^N p_X(k) \quad (13)$$

where

$$p_X(k) = U_{dc\_X}(k) i_X(k) \cdot [T_X(k) - \frac{1 - \text{sgn}(u_{\text{Xref}}(k))}{2} \cdot nT_s - \Delta T(k)] \cdot \frac{1}{T_s} \quad (14)$$

Equation (14) represents the DC power generated by one phase within one carrier-wave period.

#### 2) The method of computing DC power

A first-in first-out (FIFO) data queue is introduced to realize DC-power real-time calculation [20], as shown in Fig.2. The length of queue depends on the proportion between the fundamental period and carrier-wave period and is set to  $N$  based on the above analysis. In each  $T_s$ , a new data which calculated by (15) will be filled in the queue.

$$\begin{aligned} p_X(k+1) &= U_{dc\_X}(k+1) i_X(k+1) \cdot \\ &[T_X(k+1) - \frac{1 - \text{sgn}(u_{\text{Xref}}(k+1))}{2} \cdot nT_s - \Delta T(k+1)] \cdot \frac{1}{T_s} \end{aligned} \quad (15)$$

The DC power average power  $P_X^{\text{new}}$  will be updated as (16).

$$P_X^{\text{new}} = P_X^{\text{old}} + \frac{1}{N} [p_X(k+1) - p_X(k-N+1)] \quad (16)$$

where  $P_X^{\text{new}}$  is the average power after updating, and  $P_X^{\text{old}}$  is the average power of the previous cycle.

#### 3) The relationship between power generation ratios and DC power

The average DC power of three phases can be expressed by (17).

$$P_{\text{ave}} = \frac{(P_A + P_B + P_C)}{3} \quad (17)$$

Thus, the power generation ratios  $k_X$  ( $X=A, B, C$ ) given by (18) should satisfy (19).

$$k_A = \frac{P_A}{P_{\text{ave}}}, k_B = \frac{P_B}{P_{\text{ave}}}, k_C = \frac{P_C}{P_{\text{ave}}} \quad (18)$$

$$k_A + k_B + k_C = 3 \quad (19)$$

Equation (20) can be obtained by substituting (2), (13), and (14) into (17).

$$P_{ave} = \frac{1}{3N} \sum_{k=0}^N \sum_{X=A, B, C} \left\{ \frac{U_{dc\_X}(k) i_X(k)}{T_s} \cdot [T_X(k) - \Delta T(k) - \frac{1 - \text{sgn}[u_{Xref}(k)]}{2} \cdot nT_s] \right\}$$

$$= \underbrace{\frac{1}{3N} \sum_{k=0}^N \sum_{X=A, B, C} \left\{ U_{dc\_X}(k) i_X(k) \cdot [T_X(k) - \frac{1 - \text{sgn}(u_{Xref}(k))}{2} \cdot nT_s] \cdot \frac{1}{T_s} \right\}}_{\text{term I}} - \underbrace{\frac{1}{3N} \sum_{k=0}^N U_{dc}(k) \cdot \Delta T(k) \frac{1}{T_s} \sum_{X=A, B, C} i_X(k)}_{\text{term II}} \quad (20)$$

$$P_X = k_X P_{ave}$$

$$\Downarrow$$

$$\frac{1}{N} \sum_{k=0}^N \left\{ U_{dc\_X}(k) i_X(k) \cdot [T_X(k) - \frac{1 - \text{sgn}(u_{Xref}(k))}{2} \cdot nT_s - \Delta T(k)] \cdot \frac{1}{T_s} \right\} = k_X \frac{1}{3N} \sum_{k=0}^N \sum_{X=A, B, C} \left\{ U_{dc\_X}(k) i_X(k) \cdot [T_X(k) - \frac{1 - \text{sgn}(u_{Xref}(k))}{2} \cdot nT_s] \cdot \frac{1}{T_s} \right\}$$

$$\Downarrow$$

$$P_X^0 - \frac{1}{N} \sum_{k=0}^N [U_{dc\_X}(k) i_X(k) \cdot \Delta T(k) \cdot \frac{1}{T_s}] = k_X P_{ave}$$

$$\Downarrow$$

$$\frac{1}{N} \sum_{k=0}^N [U_{dc\_X}(k) i_X(k) \cdot \Delta T(k) \cdot \frac{1}{T_s}] = (1 - k_X) P_{ave}$$

In three-phase symmetry power systems, the sum of the three-phase currents is zero, so Term II of (20) is zero. Thus  $P_{ave}$  is only determined by DC-link voltages  $U_{dc\_X}$  and AC currents  $i_X$ , while  $\Delta T$  has no effect on it. Equation (21) which acquired by substituting (13) and (20) into (18) illustrates the relationship between  $k_X$  and  $\Delta T$ . The derivation process is presented in (21), where  $P_X$  represents the power of each phase before we control the power. In balanced three-phase symmetry power systems,  $P_X^0$  is equal to  $P_{ave}$ .

As can be seen from (21), power generation ratios  $k_X$  is only related to three variables as DC side voltages  $U_{dc\_X}$ , AC side currents  $i_X$ , and duty ratio correction  $\Delta T$ , so the DC power can be controlled by adjusting correction value  $\Delta T$ . This adjustment does not affect the average DC power of the converter.

### III. THE THREE INTER-PHASE POWER CONTROL METHODS

Based on the above analysis, the DC power can be controlled by adjusting the correction value  $\Delta T$ . Thus the control accuracy depends on the precision of  $\Delta T$ . The three calculation methods are presented as follows.

#### A. The control method based on the minimum and maximum values of $\Delta T$ (CMMM)

The following steps outline CMMM when  $k_X \neq k_X^*$ , where  $k_X^*$  is the references of DC-power ratios.

##### 1) Choosing the priority control phase

The power generation ratio deviation is defined as  $\Delta k_X = |k_X^* - k_X|$ . Since the phase with the largest value of  $\Delta k_X$  deviates maximally, it will be set as the priority control phase. And the direction of  $\Delta T$  will be decided by (22).

$$\begin{aligned} \text{if } \Delta k_A = \max(\Delta k_A, \Delta k_B, \Delta k_C), \quad \Delta T \text{ decided by A} \\ \text{if } \Delta k_B = \max(\Delta k_A, \Delta k_B, \Delta k_C), \quad \Delta T \text{ decided by B} \\ \text{if } \Delta k_C = \max(\Delta k_A, \Delta k_B, \Delta k_C), \quad \Delta T \text{ decided by C} \end{aligned} \quad (22)$$

##### 2) Comparing the expected power generation ratios and real power generation ratios

By comparing  $k_X$  with  $k_X^*$ , to increase or decrease  $p_X(k+1)$  can be determined. For example, when  $k_X$  is greater than  $k_X^*$ , the output power  $p_X$  of each phase is less than zero. In order to reach the expected value,  $p_X$  should be increased. Thus  $p_X(k+1)$  will be decided by (23) based on (12).

$$\begin{cases} \text{if } k_X > k_X^*, \quad \Delta P_X^{\text{current}} \text{ to be increased} \Rightarrow \Delta p_{X\_in} \text{ to be increased} \\ \text{if } k_X < k_X^*, \quad \Delta P_X^{\text{current}} \text{ to be decreased} \Rightarrow \Delta p_{X\_in} \text{ to be decreased} \end{cases} \quad (23)$$

##### 3) Identifying the direction of $\Delta T$ in current control period

Since the direction of  $\Delta p_{X\_in}$  has been decided by step 2), the variation trend of  $\Delta T$  in current control period is expressed by (24) based on (16).

$$\begin{cases} \text{if } k_X > k_X^* \left\{ \begin{array}{l} \Delta p_{X\_in} \text{ to be increased} \\ \text{if } \text{sgn}(i_X) > 0, \quad \Downarrow \\ \Delta T \text{ to be increased} \\ \Delta p_{X\_in} \text{ to be increased} \\ \text{if } \text{sgn}(i_X) < 0, \quad \Downarrow \\ \Delta T \text{ to be decreased} \end{array} \right. \end{cases} \quad (24\text{-a})$$

$$\begin{cases} \text{if } k_X < k_X^* \left\{ \begin{array}{l} \Delta p_{X\_in} \text{ to be decreased} \\ \text{if } \text{sgn}(i_X) > 0, \quad \Downarrow \\ \Delta T \text{ to be decreased} \\ \Delta p_{X\_in} \text{ to be decreased} \\ \text{if } \text{sgn}(i_X) < 0, \quad \Downarrow \\ \Delta T \text{ to be increased} \end{array} \right. \end{cases} \quad (24\text{-b})$$

##### 4) Identifying the value of $\Delta T$ in current control period

According to the previous analysis, the range of  $\Delta T$  is  $[\Delta T_{min} \Delta T_{max}]$ . So the value of  $\Delta T$  is decided by (25).

$$\begin{aligned} \text{if } \Delta T \text{ to be increased} &\Rightarrow \Delta T = \Delta T_{max} \\ \text{if } \Delta T \text{ to be decreased} &\Rightarrow \Delta T = \Delta T_{min} \end{aligned} \quad (25)$$

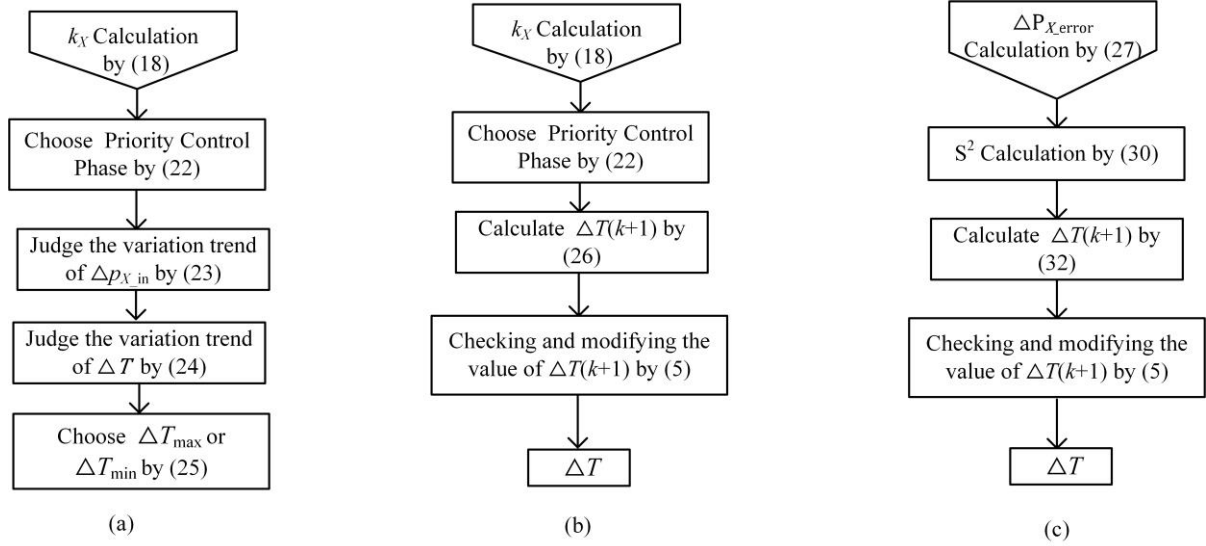


Fig. 3 Flow chart of proposed methods. (a) CMMM, (b) CMPP, (c) CMMV.

So far, CMMM algorithm has been fulfilled and the flow chart of CMMM is shown in Fig.3(a).

### B. The control method based on the control priority phase (CMPP)

CMMM is intuitive, but there is no unified formula to calculate the  $\Delta T$ . So we analyze the relationship between  $\Delta T$  and power generation ratios and give a formula for  $\Delta T$ .

#### 1) Choosing the control priority phase

The first step is to choose the priority control phase used to calculate the  $\Delta T$ , which is the same as CMMM.

#### 2) Calculating the value of $\Delta T$

To achieve the inter-phase power control, we calculate the  $\Delta T(k+1)$  to make the actual power equal to the expected one.

By combining (15), (16) and (18),  $\Delta T(k+1)$  can be acquired by (26)

$$\Delta T(k+1) = T_x(k+1) - \frac{1 - \text{sgn}[u_{\text{Aref}}(k+1)]}{2} n T_s - \frac{T_s [N(k_x^* P_{\text{ave}} - P_x^{\text{old}}) + p_x(k-N+1)]}{U_{\text{dc}_x}(k+1) i_x(k+1)} \quad (26)$$

#### 3) Checking and modifying the value of $\Delta T$

$\Delta T(k+1)$  should satisfy equation (5) to comply with linear modulation. When  $\Delta T(k+1)$  reaches the limit of the  $[\Delta T_{\min}, \Delta T_{\max}]$ , it should take the value of  $\Delta T_{\min}$  or  $\Delta T_{\max}$  accordingly. So far, CMPP algorithm can be fulfilled and the flow chart of CMPP is shown in Fig.3(b).

### C. The control method based on minimizing the variances of three-phase power (CMMV).

In order to gain better steady state performance of DC power control,  $\Delta T(k+1)$  should precisely satisfy the three-phase power generation ratios simultaneously. Thus,  $\Delta T(k+1)$  can be calculated by minimizing the variances of the three-phase power.  $\Delta P_{\text{xerror}}$  is the error between the actual and the expected power of each phase. CMMV is presented as follow.

$\Delta P_{\text{xerror}}$  can be expressed by (27).

$$\Delta P_{\text{xerror}} = P_x^{\text{old}} + \frac{1}{N} [p_x(k+1) - p_x(k-N+1)] - k_x^* P_{\text{ave}} \quad (27)$$

Thus, the variance of three-phase power is given by (28).

$$\begin{aligned} S^2 &= \Delta P_{\text{Aerror}}^2 + \Delta P_{\text{Berror}}^2 + \Delta P_{\text{Cerror}}^2 \\ &= (P_A^{\text{old}} + \frac{1}{N} [p_A(k+1) - p_A(k-N+1)] - k_A^* P_{\text{ave}})^2 \\ &\quad + (P_B^{\text{old}} + \frac{1}{N} [p_B(k+1) - p_B(k-N+1)] - k_B^* P_{\text{ave}})^2 \\ &\quad + (P_C^{\text{old}} + \frac{1}{N} [p_C(k+1) - p_C(k-N+1)] - k_C^* P_{\text{ave}})^2 \end{aligned} \quad (28)$$

According to equation (15),  $p_x(k+1)$  can be expressed as (29).

$$p_x(k+1) = u_{\text{xref}}^*(k+1) i_x(k+1) - \frac{U_{\text{dc}}(k+1) i_x(k+1) \Delta T(k+1)}{T_s} \quad (29)$$

Thus, equation (28) can be rewritten as (30).

$$\begin{aligned} S^2 &= \left( P_A^{\text{old}} + \frac{[u_{\text{Aref}}^*(k+1) i_A(k+1) - \frac{U_{\text{dc}}(k+1) i_A(k+1) \Delta T(k+1)}{T_s} - p_A(k-N+1)]}{N} - k_A^* P_{\text{ave}} \right)^2 \\ &\quad + \left( P_B^{\text{old}} + \frac{[u_{\text{Bref}}^*(k+1) i_B(k+1) - \frac{U_{\text{dc}}(k+1) i_B(k+1) \Delta T(k+1)}{T_s} - p_B(k-N+1)]}{N} - k_B^* P_{\text{ave}} \right)^2 \\ &\quad + \left( P_C^{\text{old}} + \frac{[u_{\text{Cref}}^*(k+1) i_C(k+1) - \frac{U_{\text{dc}}(k+1) i_C(k+1) \Delta T(k+1)}{T_s} - p_C(k-N+1)]}{N} - k_C^* P_{\text{ave}} \right)^2 \end{aligned} \quad (30)$$

Equation (30) indicates that  $S^2$  is a quadratic function of  $\Delta T(k+1)$ , and the opening is upward, so that the minimum duty ratio of the squared sum of the above power deviation is the duty ratio correction sought, namely, the extreme point above function. Thus, the extreme point can be acquired by (31), and can be simplified as (32).  $\Delta T$  can be used to control the DC power directly after a threshold processing.

$$\frac{d(S^2)}{d(\Delta T)} = 0 \quad (31)$$

$$\Delta T(k+1) = \frac{T_s N}{U_{dc}(i_A(k+1)^2 + i_B(k+1)^2 + i_C(k+1)^2)} * \left( \begin{aligned} & (P_A^{old} i_A(k+1) + P_B^{old} i_B(k+1) + P_C^{old} i_C(k+1)) \\ & + \frac{1}{N} [u_{Aref}^*(k+1) i_A(k+1) - p_A(k-N+1)] * i_A(k+1) - k_A^* P_{ave} * i_A(k+1) \\ & + \frac{1}{N} [u_{Bref}^*(k+1) i_B(k+1) - p_B(k-N+1)] * i_B(k+1) - k_B^* P_{ave} * i_B(k+1) \\ & + \frac{1}{N} [u_{Cref}^*(k+1) i_C(k+1) - p_C(k-N+1)] * i_C(k+1) - k_C^* P_{ave} * i_C(k+1) \end{aligned} \right) \quad (32)$$

So far, three algorithms have been fulfilled and the flow charts are shown in Fig.3.

#### IV. THE INNER-PHASE POWER CONTROL METHOD

Unbalanced power not only exists in inter phase but also comes out in inner phase. Thus, there is a need for a method that can control the power distribution of the inner phase to further improve the power controllability of the system. This paper proposes an inner-phase power control method to achieve power distribution by using the inner-phase duration correction value  $\Delta D_{Xi}$ , which is similar to the inter-phase power control methods.

The inner phase power generation ratios can be expressed as (33), where  $P_{Xave}$  is the average power of all submodules in a phase,  $P_{Xi}$  represents the DC power of submodule  $i$  of phase  $X$  in a fundamental period.

$$l_{Xi} = \frac{P_{Xi}}{P_{Xave}} \quad (33)$$

According to (14), the revised duration time of one phase can be expressed as (34).

$$D(X) = T_s(k) - \frac{1 - \text{sgn}(u_{Xref}(k))}{2} \cdot nT_s - \Delta T(k) \quad (34)$$

When the duration times distribute equally among the submodules, the DC power generated by one submodule within  $T_s$  can be expressed as (35), where  $\Delta D_{Xi}$  is the correction value injected in submodule  $i$  of phase  $X$ , and it should satisfy  $\Delta D_{X1} + \Delta D_{X2} + \dots + \Delta D_{Xn} = 0$ , so as not to affect the duration time of one phase.

$$p_{Xi}(k) = U_{dc}(k) i_{Xi}(k) \cdot \left[ \frac{D(X)}{n} - \Delta D_{Xi}(k) \right] \cdot \frac{1}{T_s} \quad (35)$$

Similar to the inter-phase power control, the relationship between the carrier-wave period DC power and the fundamental period DC power can be expressed as (36).

$$p_{Xi}(k+1) = N(P_{Xi}^* - P_{Xi}^{old}) + p_{Xi}(k-N+1) \quad (36)$$

Combining (33), (35) and (36), the correction value of each submodule can be expressed as (37).

$$\Delta D_{Xi}(k+1) = \frac{D(X)}{n} - \frac{N(l_{Xi}^* P_{Xave} - P_{Xi}^{old}) + p_{Xi}(k-N+1)}{U_{dc}(k+1) i_{Xi}(k+1)} T_s \quad (37)$$

Therefore, the correction values can be obtained according to the inner phase power generation ratios  $l_{Xi}^*$ , and it can be

used to control the inner phase power directly without affecting the inter phase power.

Briefly, the inner phase power control is achieved by changing the pulse distribution of each submodule. However, it should be noted that adopting inter-phase and inner-phase power control will lead to the increase of the switching frequency.

#### V. THE CONTROL LIMITATION OF POWER GENERATION RATIOS

With three inter-phase power control methods, power generation ratio of each phase will be distributed following the expected value, but the power regulation range is limited. The limitation will be analyzed to ensure the expansibility and applicability.

From (21), the adjustable DC power within one control period is shown as (38). According to equation (22), inter-phase power control can be achieved through controlling and adjusting  $\Delta T$ .

$$\Delta p_X(k) = U_{dc-X}(k) i_X(k) \cdot \Delta T(k) / T_s \quad (38)$$

Thus the adjustable DC power  $\Delta P_X$  within  $T_{fund}$  can be expressed as (39).

$$\Delta P(k) = \frac{1}{N} \sum_{k=0}^N \Delta p_X(k) \quad (39)$$

Power generation ratios  $k_X$  in (18) can be rewritten as

$$k_X = \frac{P_{ave} - \Delta P_X}{P_{ave}} \quad (40)$$

Therefore, ranges of  $\Delta P_X$  will be analyzed to obtain the power generation ratios limitation.

For simplicity, the upper and lower limit of  $\Delta P_A$  can be obtained assuming  $\text{sgn}(u_{Aref}) = \text{sgn}(i_A)$  and  $k_A > k_A^*$ . Therefore, (41) can be established to derive the limitation of  $\Delta P_A$  based on (32), (38), and (39).

$$\Delta T_j = \begin{cases} \Delta T_{max}, \text{sgn}(i_A) = 1/0 \\ \Delta T_{min}, \text{sgn}(i_A) = -1 \end{cases} \quad (41)$$

The maximum value  $\Delta P_{max\_A}$  can be expressed by (42),

$$\begin{aligned} \Delta P_{max\_A} &= \frac{1}{T} \int_0^{\pi} U_{dc\_A} \frac{u_{Aref}}{Z} \cdot \Delta T_{max} d\omega + f_{fund} \int_{\pi}^{2\pi} U_{dc\_A} \frac{u_{Aref}}{Z} \cdot \Delta T_{min} d\omega \\ &= \underbrace{\frac{1}{T} \int_0^{\pi} U_{dc\_A} \frac{U_{dc\_A} m \sin(\omega t)}{Z} \cdot \Delta T_{max} d\omega}_{\text{Term 1}} + \underbrace{\frac{1}{T} \int_{\pi}^{2\pi} U_{dc\_A} \frac{U_{dc\_A} m \sin(\omega t)}{Z} \cdot \Delta T_{min} d\omega}_{\text{Term 2}} \end{aligned} \quad (42)$$

where  $Z$  is the impedance of the grid side, and  $u_{Aref}$  ( $u_{Aref} = U_{dc\_A} \cdot m \cdot \sin(\omega t)$ ) is the reference signal of phase A,

$$\begin{aligned} \Delta T_{max} &= \min(T_A, T_B, T_C) = \min \left\{ mT_s \sin(\omega t) + \frac{1 - \text{sgn}[\sin(\omega t)]}{2} \cdot nT_s, \right. \\ & \quad mT_s \sin(\omega t - 2\pi/3) + \frac{1 - \text{sgn}[\sin(\omega t - 2\pi/3)]}{2} \cdot nT_s, \\ & \quad \left. mT_s \sin(\omega t + 2\pi/3) + \frac{1 - \text{sgn}[\sin(\omega t + 2\pi/3)]}{2} \cdot nT_s \right\} \end{aligned} \quad (43)$$



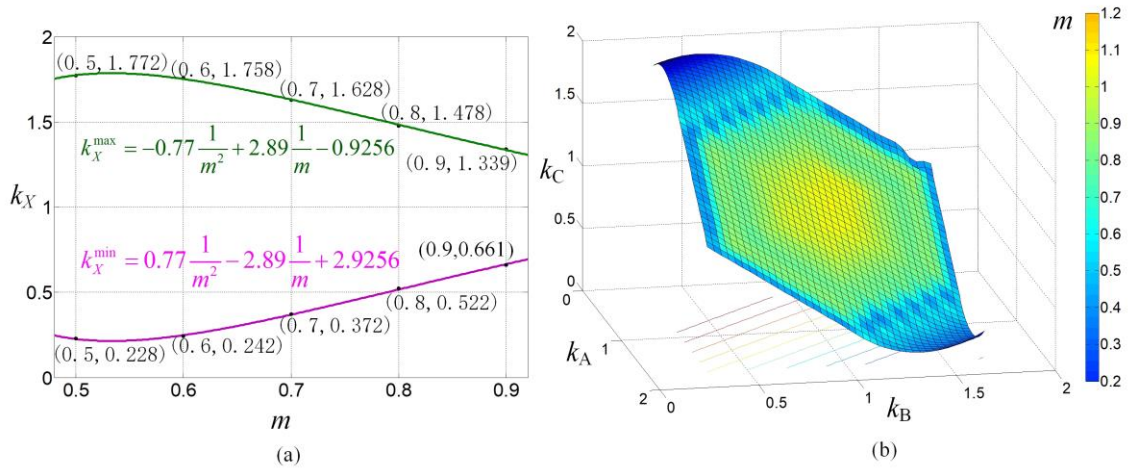


Fig. 4 The limit of the reference power generation ratios  $k_x^*$ . (a) Two-dimensional graph. (b) Three-dimensional graph.

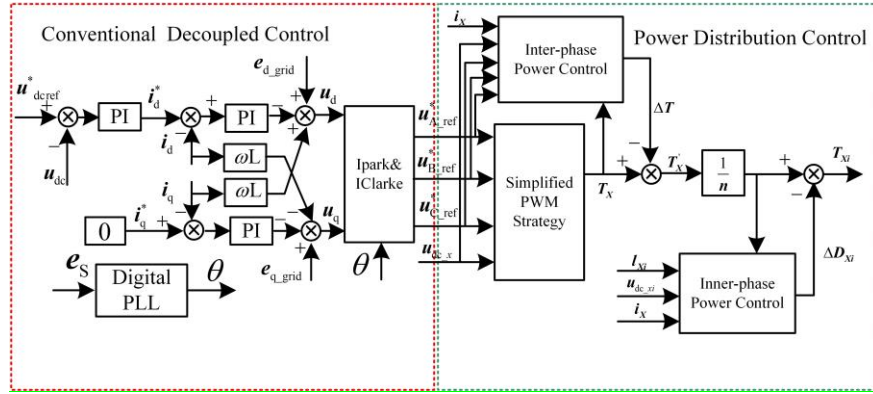


Fig. 5 Control block diagram of the grid-connected inverter system.

By analyzing (42) and (43), it can be found that Term 1 and  $m$  can be related in quadratic function after the integral calculation. Term 2 can also be analyzed similarly. Consequently,  $\Delta P_{\max\_A}$  and  $m$  obey (45), where  $a$ ,  $b$ , and  $c$  are coefficients.

$$\text{Term 1} = \frac{1}{T} \int_0^{\pi} U_{dc\_A} \frac{U_{dc\_A} m \sin(\omega t)}{Z} \cdot \min(T_A, T_B, T_C) d\omega t \quad (44)$$

$$\Delta P_{\max\_A} = am^2 + bm + c \quad (45)$$

$P_{ave}$  is a quadratic function of  $m$ , as shown in (46). So the relation of  $k_{\min\_A}^*$  and  $m$  can be expressed by (47). Adopting the same method,  $k_{\max\_A}^*$  can be easily attained as well.

$$P_{ave} = dm^2 \quad (46)$$

$$k_{\min\_A}^* = \frac{P_{ave} - \Delta P_{\max\_A}}{P_{ave}} = \left(1 - \frac{a}{d}\right) - \frac{b}{dm} - \frac{c}{dm^2} \quad (47)$$

According to (47), power generation ratio is a quadratic function of the reciprocal  $1/m$ . Three special power points can be used to solve equation (47). The relationship between  $m$  and three-phase generation ratios are drawn in Fig.4. Fig.4(a) shows the corresponding relationship between the limit of the reference generation ratio  $k_X^*$  ( $X = A$  or  $B$  or  $C$ ) and  $m$ , indicating that the reference generation ratio of each phase is acceptable within this range. At the same time, three-phase generation ratios must satisfy (19). In order to show the relationship between  $k_X^*$  and  $m$  as well as the three-phase generation ratios at the same time, a three-dimensional graph

is drawn as in Fig.4(b). This three-dimensional graph is obtained by fitting the simulation data, since a unified mathematical expression has not been found at present. It can be seen that when  $m$  is 1, three-phase power generation ratios concentrate in the middle area of the three-dimensional graph, so the adjustable range is small. When  $m$  is 0.5, three-phase power generation ratios are distributed around the three-dimensional graph, so the adjustable range is large. It can be concluded that the active power control capability becomes weaker as modulation index  $m$  increases.

It is observed from the above analysis that the theoretical power generation ratios limitation is determined by modulation index  $m$ . If only the power generation ratios are within this theoretical range, the DC power can be controlled as expected.

TABLE I  
PARAMETER SETTINGS FOR SIMULATIONS AND EXPERIMENTS  
IN LOW POWER SYSTEMS

Parameter	Value
Voltage of Battery Cells	48V
DC-link Capacitor	1200 $\mu$ F
L filter	4mH
Switching Frequency	8kHz
Chain number per phase	2
Rated Power	465W



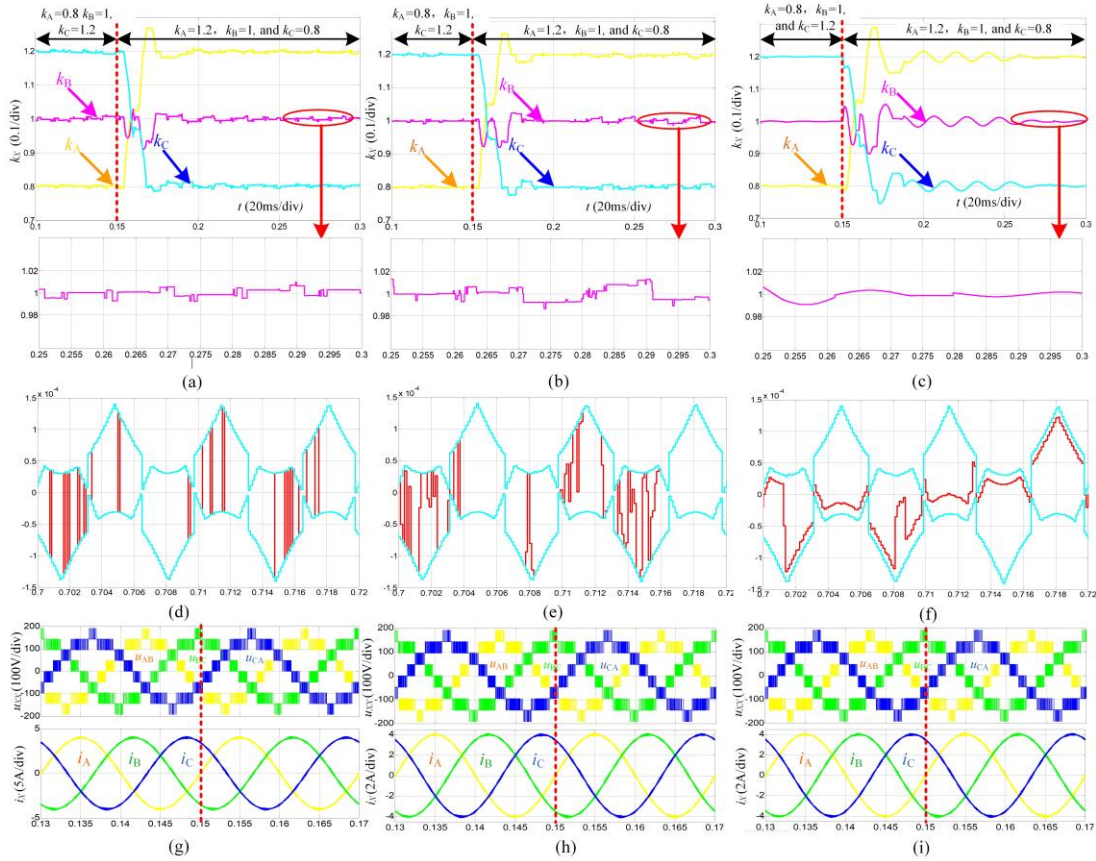


Fig. 6 Simulation results in low power systems with CMMM, CMPP, and CMMV, respectively. (a)~(c) Power generation ratios  $k_x$ . (d)~(f) The steady-state waveform of  $\Delta T$ . (g)~(i) Converter output voltages  $u_{xx}$  and output AC currents  $i_x$ .

## VI. SIMULATION AND EXPERIMENT

Fig.5 shows the control block diagram of grid-connected inverter. The whole control is divided into two subs controls: 1) Conventional decoupled control based on the  $dq$  rotational frame; 2) Power distribution control using proposed methods.

### A. Simulation and analysis

#### 1) Simulation results of CMMM, CMPP, and CMMV in low power systems

A three-phase five-level CHB grid-connected inverter is simulated in MATLAB/Simulink to compare the proposed three methods. The system parameters are shown in Table I and the simulation results are shown in Fig.6.

Fig.6(a)~(c) show the simulation waveform of CMMM, CMPP, and CMMV with the power generation ratios ranging from  $(k_A^*/k_B^*/k_C^*=0.8/1/1.2)$  to  $(k_A^*/k_B^*/k_C^*=1.2/1/0.8)$ , where the modulation index  $m$  is 0.89 and the output active power is 465W. As can be seen from Fig.6(a), (b), and (c), the three power control methods can reach the expected power generation ratios, in which CMMM and CMPP can achieve fast control, while CMMV is more precise and smoother. This can be explained by Fig.6(d), (e), and (f) which show the waveforms of correction time  $\Delta T$  in the steady state. It should note that the value of  $\Delta T$  is shown in red line, and the maximum and minimum allowable values of  $\Delta T$  are shown in

blue line, as observed using a uniform zero baseline. In Fig.6 (d), the waveform of  $\Delta T$  switches between the upper and lower limits, causing the real-time DC power in CMMM to fluctuate. Power control with CMPP, as in Fig.6(e), is not smooth, for the correction time  $\Delta T$  always exceeds the limiting value and thus should be limited. In Fig.6(f),  $\Delta T$  falls within the limiting values and is continuous, indicating that  $\Delta T$  can satisfy the three-phase power equation in CMMV. It is then concluded that CMMV can realize more accurate and smoother control of DC power. In addition, CMMM and CMPP select the phase whose power deviation is largest as the priority control phase, thus the fast control can be obtained. Since CMMV is a method that minimizes the total deviation of three-phase power, it takes more time to reach the steady state. Fig.6(g), (h), and (i) show the waveforms of line-to-line voltages  $u_{xx}$  and AC currents  $i_x$  of CMMM, CMPP, and CMMV, respectively. It indicates that the high quality voltages and currents can be obtained with these methods, and the switching of power generation ratios has little effect on them.

#### 2) Simulation results of CMMM, CMPP, and CMMV in high power systems

To verify the feasibility of three inter-phase power control methods in high power systems, the simulations with power generation ratios ranging from  $(k_A^*/k_B^*/k_C^*=1.2/1/0.8)$  to  $(k_A^*/k_B^*/k_C^*=0.8/1/1.2)$  are implemented in the 10-cell CHB converter, where the modulation index  $m$  is 0.89 and the output active

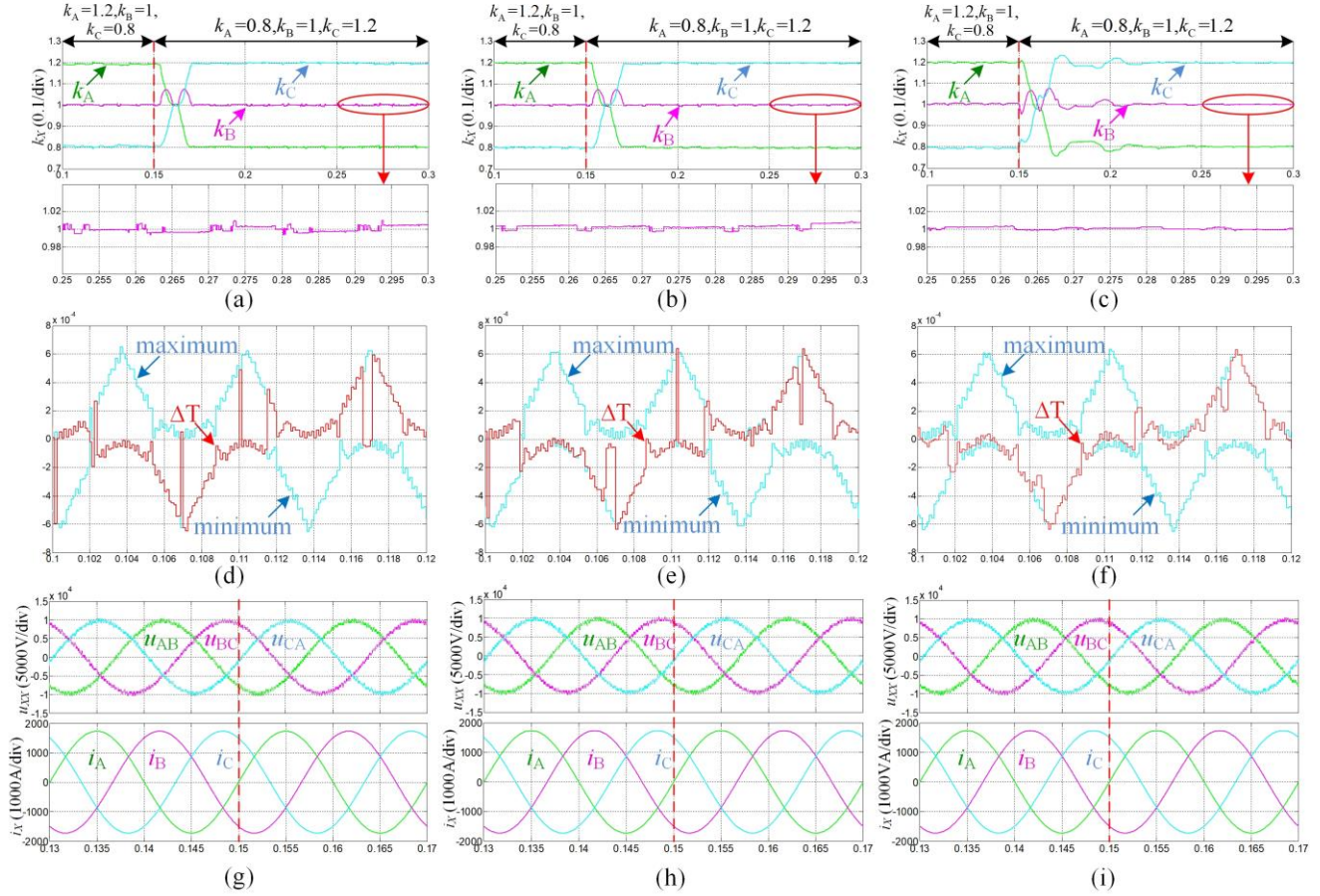


Fig. 7 Simulation results in high power systems with MMM, CMPP, and CMMV, respectively. (a)~(c) Power generation ratios  $k_x$ . (d)~(f) The steady-state waveform of  $\Delta T$ . (g)~(i) Converter output voltages  $u_{xy}$  and output AC currents  $i_x$ .

power is 10MW. The simulation parameters are shown in Table II and the simulated results are shown in Fig.7. It is clear from the figures that three control methods can achieve high precise control of DC power, and the simulation results are similar to those in low power systems.

TABLE II  
PARAMETER SETTINGS FOR SIMULATIONS IN HIGH POWER SYSTEMS

Parameter	Value
Voltage of Battery Cells	577V
DC-link Capacitor	1200μF
L filter	4mH
Switching Frequency	8kHz
Chain number per phase	10
Rated Power	10MW

TABLE III  
DIFFERENCES AMONG THREE INTER-PHASE POWER CONTROL METHODS

Difference	CMMM	CMPP	CMMV
Stable speed	Rapid (0.05s)	Rapid (0.03s)	relatively slow(0.11s)
Stable state	slight fluctuation	slight fluctuation	smooth
Control precision	slight deviation( $\pm 0.01$ )	slight deviation( $\pm 0.015$ )	high precision( $\pm 0.003$ )

Comparing the above simulation results, we find that, among three inter-phase power control methods, the performances in the dynamic and steady states differ. Table III illustrates their differences by presenting the main characteristics of the three methods.

### 3) Simulation results of the method merging CMPP and CMMV (MCC)

In order to obtain good performance both in dynamic and steady states, the CMPP and CMMV are combined to form a new control strategy MCC.

By analyzing the variances of three-phase power  $S^2$ , we find that 0.01 is the critical point which can be used to decide the control strategy switch point. When  $S^2$  is greater than 0.01,  $\Delta T$  is calculated using CMPP. Otherwise, the CMMV is adopted to acquire the  $\Delta T$ . The flow chart of method MCC is shown in Fig.8.

The simulation is conducted in a five-level CHB grid-connected inverter. Table I and Fig.9 show the simulation parameters and the simulation results, respectively, to make a comparison between DMM in [11] and MCC.

Fig.9(a) and (b) show the working process of DMM and MCC with the power generation ratios ranging from  $(k_A^*/k_B^*/k_C^* = 0.8/1/1.2)$  to  $(k_A^*/k_B^*/k_C^* = 1.2/1/0.8)$ , and partial waveforms of  $k_B$  are enlarged to highlight their characteristics.



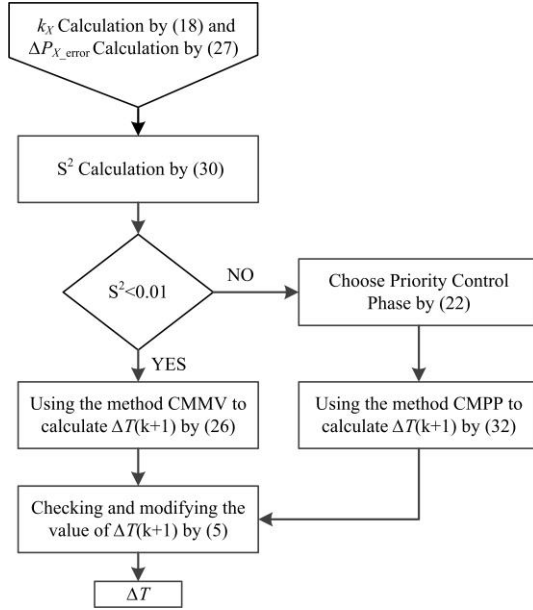


Fig. 8 The flow chart of method MCC

It can be seen that both DMM and MCC can achieve high precision in controlling DC power with the maximal deviation

less than 0.005. Compared with DMM, the convergence speed of MCC is relatively slow;  $k_B$  in MCC fluctuates around the expected value during the time from 0.25s to 0.3s. However,  $k_B$  in MCC can be stabilized to 1 during the time 0.75s-0.8s, as can be seen from Fig.9(b). This means that the deviation will become smaller along with time. In Fig.9(a), however,  $k_B$  in DMM still deviates from the expected value during the time 0.75s-0.8s. This is because the DMM uses the power of grid side instead of the converter side, so the reactive power raised by the L filter is unnecessary included in the calculation. Such difference tends to be small as the value of the L filter is small. Still this will lead to error while controlling the power of the three phases. It will be worse when the L filter is large under certain circumstances. In MCC, the output DC power is completely calculated by the converter side, so the power generation ratios can reach and stabilize at the given values. Fig.9(c) and (d) show the simulation results of converter output voltages  $u_{XX}$  and grid currents  $i_X$ . The high quality output voltages and currents verify the effectiveness of DMM and MCC for DC power control.

In order to verify the cause of the power deviation in DMM, the simulation is implemented with the value of L filter impedance increasing from 4mH to 8mH, while the other conditions remain unchanged. The results are shown in Fig.10.

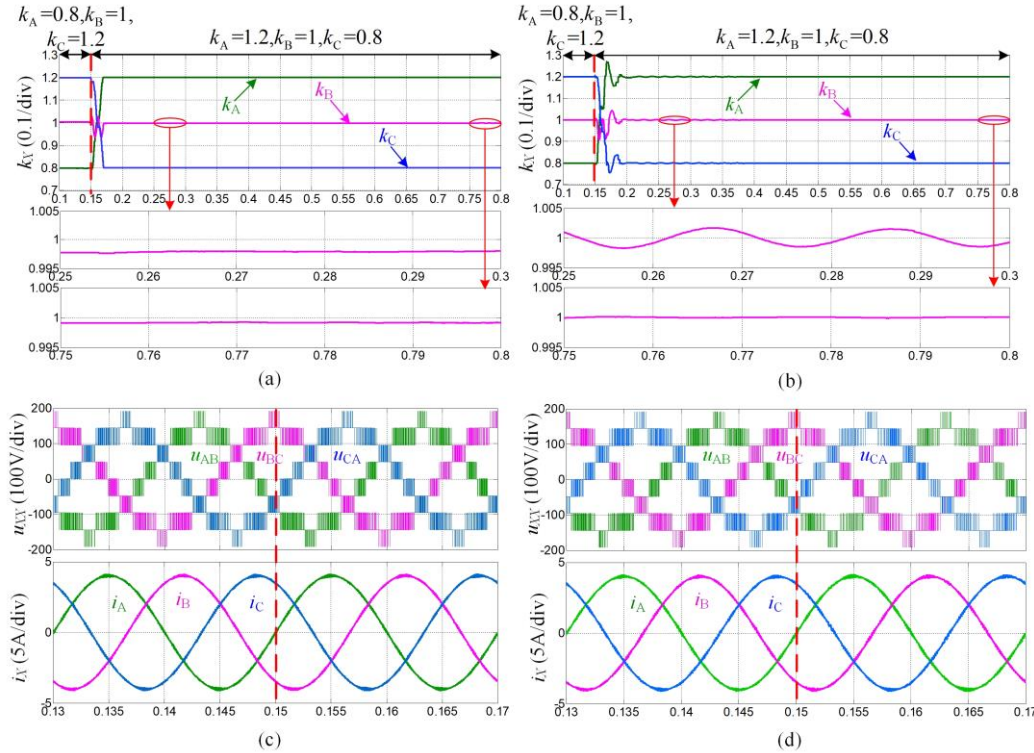


Fig. 9 Simulation results under L=4mH. (a)~(b) Power generation ratios  $k_x$  with DMM and MCC, respectively. (c)~(d) Converter output voltages  $u_{XX}$  and output AC currents  $i_X$  with DMM and MCC, respectively.

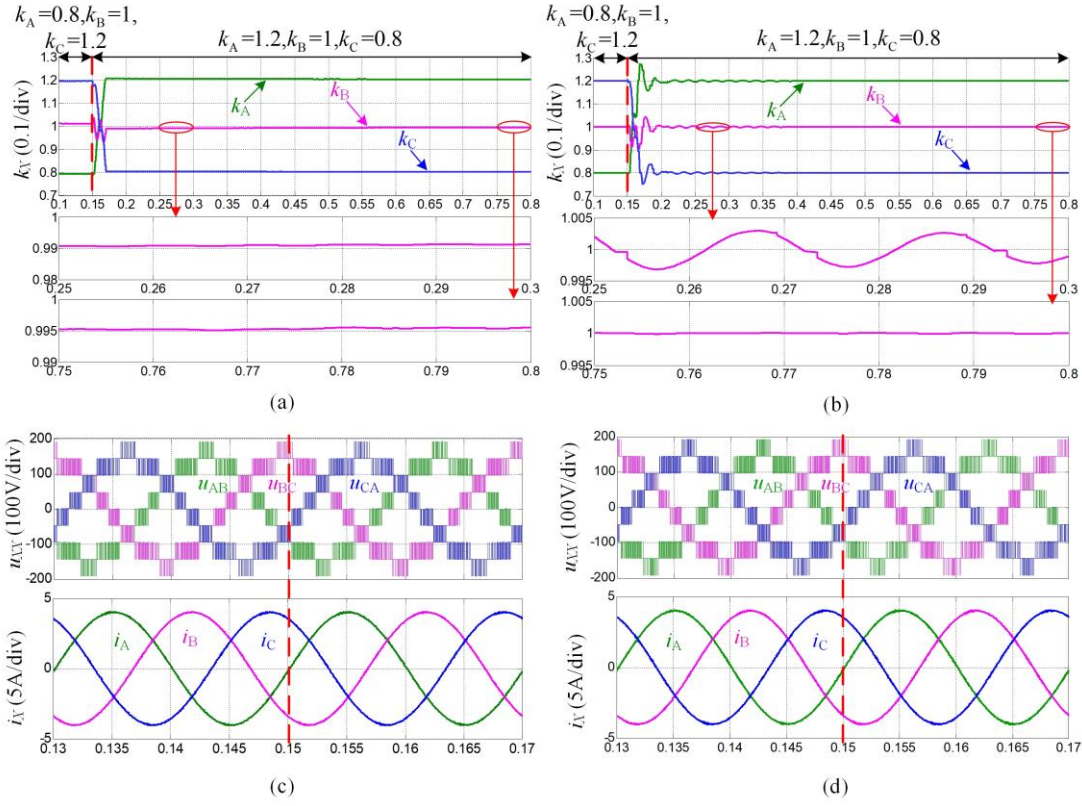


Fig. 10 Simulation results under  $L=8\text{mH}$ . (a)~(b) Power generation ratios  $k_x$  with DMM and MCC, respectively. (c)~(d) Converter output voltages  $u_{xx}$  and output AC currents  $i_x$  with DMM and MCC, respectively.

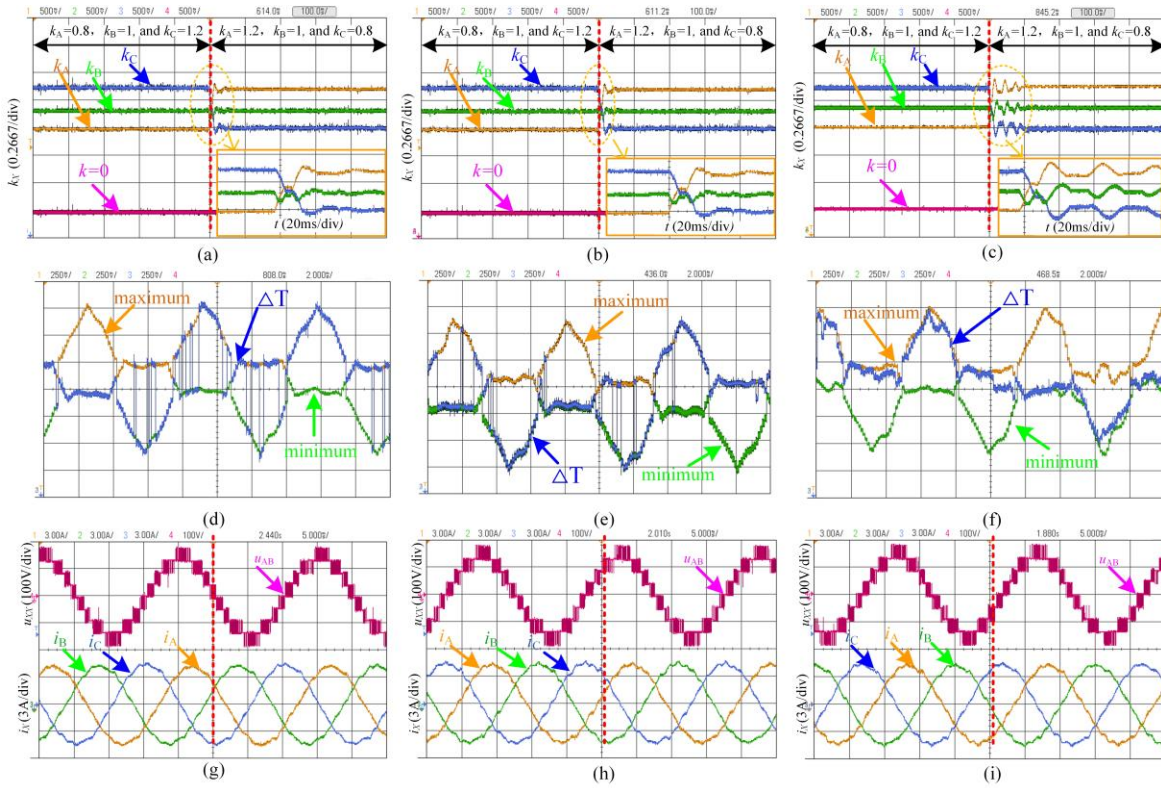


Fig. 11 Experimental results of CMMM, CMPP, and CMMV, respectively. (a)~(c) Power generation ratios  $k_x$ . (d)~(f) The steady state waveform of  $\Delta T$ . (g)~(i) Converter output voltage  $u_{AB}$  and output AC currents  $i_x$ .



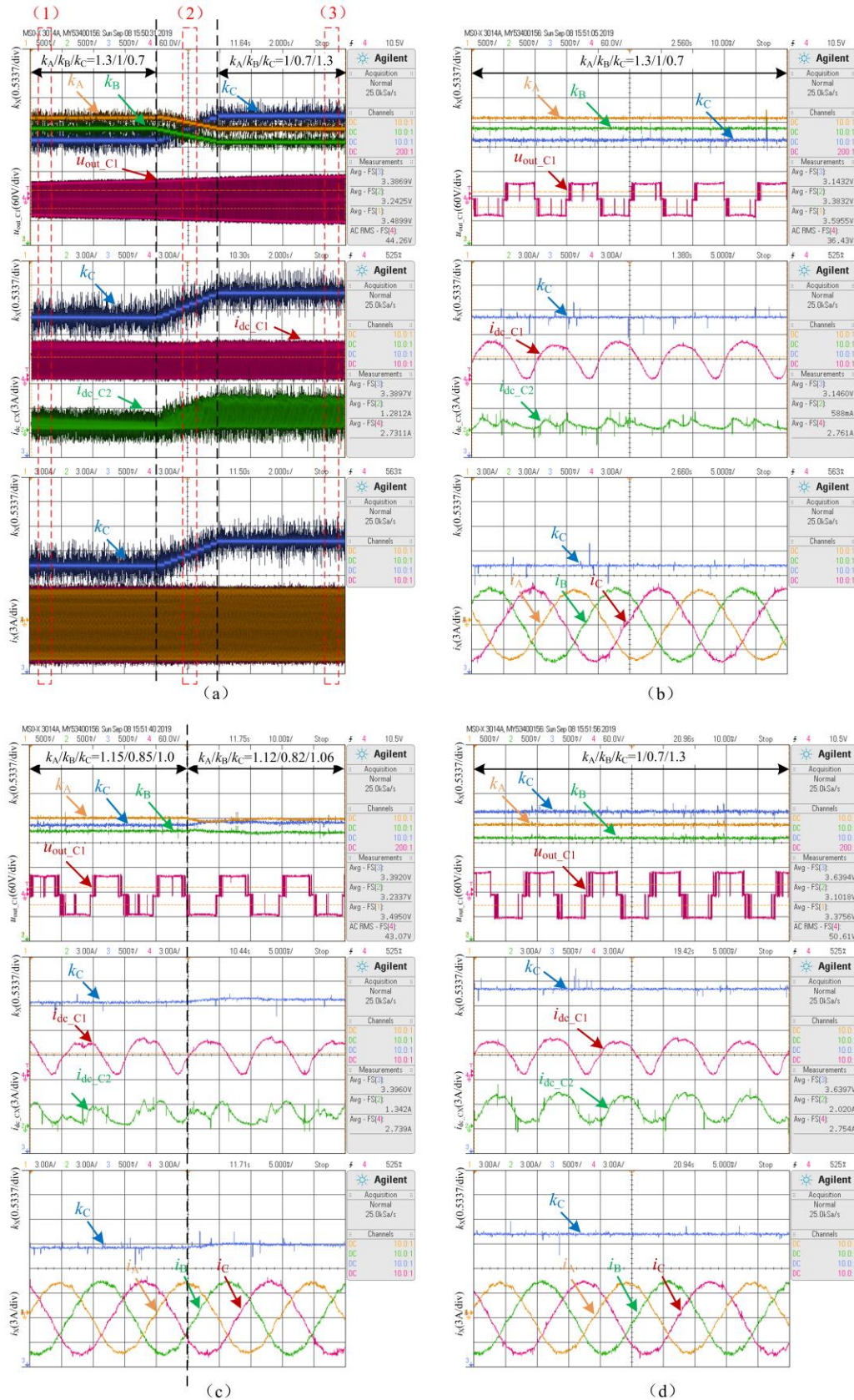


Fig. 12 Experimental results of MCC with power generation ratios ranging from  $(k_A^*/k_B^*/k_C^* = 1.3/1/0.7)$  to  $(k_A^*/k_B^*/k_C^* = 1/0.7/1.3)$ . (a) The overall waveforms. (b)~(d) The partial enlarged images of red dotted frames (1), (2) and (3) in Fig 12(a).

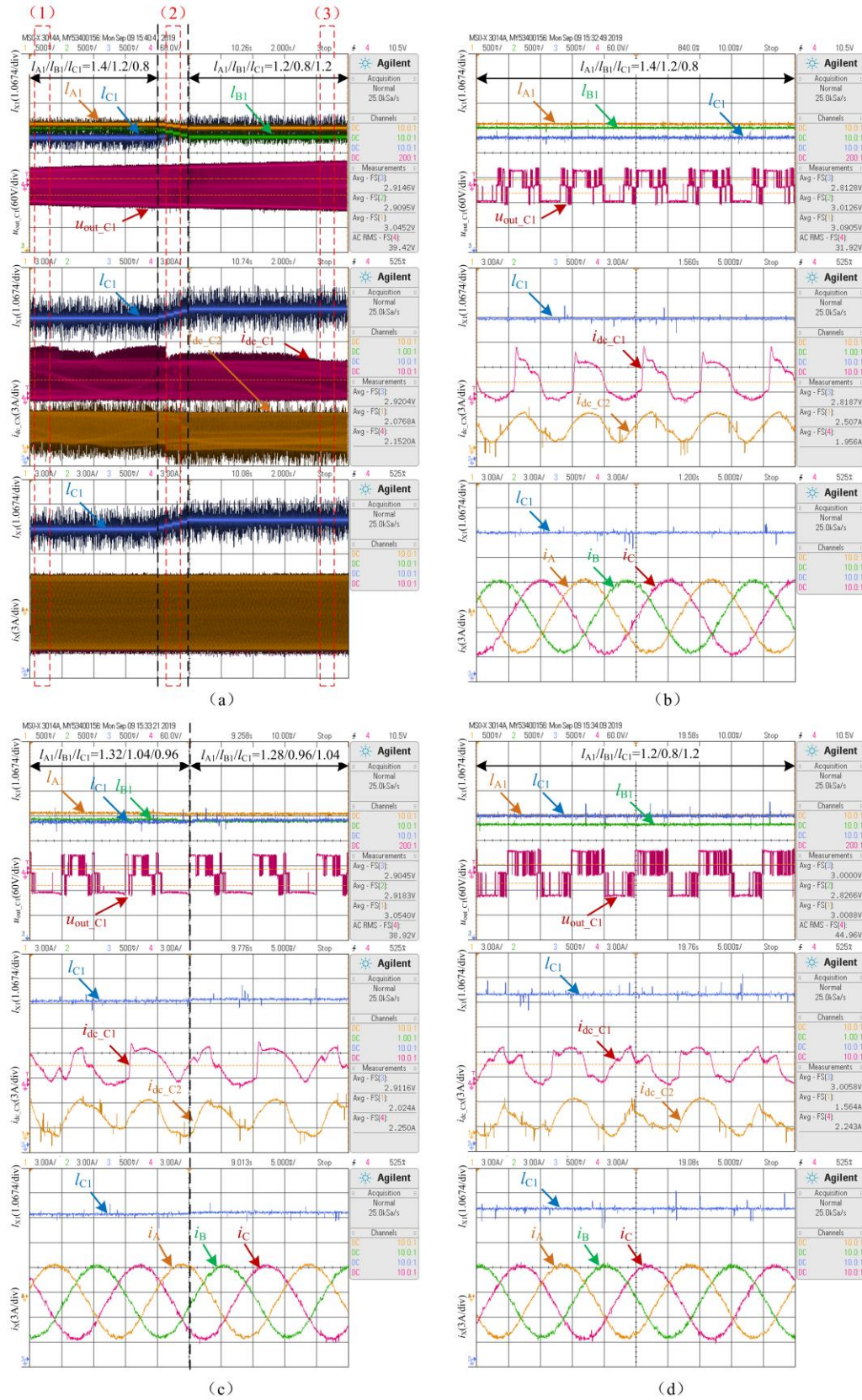


Fig. 13 Experimental results of MCC with inner-phase power coefficients ranging from  $(I_{A1}/I_{B1}/I_{C1} = 1.4/1.2/0.8)$  to  $(I_{A1}/I_{B1}/I_{C1} = 1.2/0.8/1.2)$ . (a) The overall waveforms. (b)~(d) The partial enlarged images of red dotted frames (1), (2) and (3) in Fig 13(a).



It can be seen from Fig.10(a) that the deviation of  $k_B$  in DMM is close to 0.01 during the time 0.25s-0.3s, which is much bigger than that under  $L=4\text{mH}$ , and  $k_B$  still has a deviation of approximately 0.005 at 0.75s to 0.8s, meaning that it can't reach the expected value. In MCC, the maximum deviation of  $k_B$  is less than 0.005 at 0.25s to 0.3s, and  $k_B$  can stabilize at the expected values during the time 0.75s-0.8s, as shown in Fig.10 (b). Fig.10(c) and (d) show that the output line-to-line voltages and three-phase currents in both DMM and MCC are not affected as  $L$  increases. The simulation results indicate that the deviation of DC power in DMM will increase as  $L$  increases. It can be concluded that the DC power calculated by DMM is inaccurate.

## B. Experimental results and analysis

### 1) Experimental results of three inter-phase power control methods (CMMM, CMPP, and CMMV)

A downscale grid-connected inverter is developed in lab to verify the performance both in dynamic and steady states of proposed three methods. The parameters are the same as Table I. The filter available in our laboratory is an L filter, whose impedance is a little larger than expected. Since the Per-unit design is used in the lower power system in the experiment, its transfer function can represent and is also applicable to its count part in high power system. The control methods are implemented by TMS320F28335 with Xilinx FPGA, with the reference value of  $i_d^*4\text{A}$ , the output active power about 465W, and the modulation index  $m$  about 0.89. Fig.11(a), (b), and (c) show the whole working process of three power control methods with the power generation ratios ranging from  $(k_A^*/k_B^*/k_C^*=0.8/1/1.2)$  to  $(k_A^*/k_B^*/k_C^*=1.2/1/0.8)$ . It can be seen that the power generation ratios of three control methods can reach the expected value accurately, where CMMM and CMPP take about 20ms to reach the steady state after the power generation ratios are switched, while CMMV takes about 80ms. Fig.11(d), (e), and (f) show the waveforms of correction time  $\Delta T$  calculated by three methods in the steady state. Similar to the simulation results, the waveforms of  $\Delta T$  in CMMM and CMPP are discontinuous and switch between the maximum and minimum values. In CMMV,  $\Delta T$  is a continuous value and is restricted within the limit values, indicating that CMMV can achieve the smooth control of DC power. Fig.11(g), (h), and (i) show the waveforms of line-to-line voltage  $u_{AB}$  and three-phase currents  $i_X$  in the AC side of the inverter system. The figure shows that balanced AC currents can be obtained as power generation ratios change. However, the AC currents  $i_X$  are distorted slightly in the overall waveforms. That is because the capacity of the experimental platform is small as 465VA, which is easily interfered by saturation voltage of IGBT, lead-acid battery impedance, etc.

### 2) Experimental results of the inter-phase power control method which merged CMMV and CMPP (MCC)

In order to examine the inter-phase power control of the MCC with imbalanced voltages, an experiment on five-level inverters is carried out. An adjustable DC voltage source available in our lab is used as the substitute of the upper battery module in phase C. The output voltage of this

equipment is changed manually during the experiment. Meanwhile, the power generation ratios are changed from  $(k_A^*/k_B^*/k_C^*=1.3/1/0.7)$  to  $(k_A^*/k_B^*/k_C^*=1/0.7/1.3)$ .

Fig.12(a) shows the overall waveforms of three-phase power generation ratios  $k_A$ ,  $k_B$  and  $k_C$ , the output voltage  $u_{\text{out}_C1}$  of the upper module in phase C, the current of adjustable voltage source in phase C  $i_{\text{dc}_C1}$ , the battery current of lower module in phase C  $i_{\text{dc}_C2}$  and three-phase currents  $i_A$ ,  $i_B$  and  $i_C$  of the power grid side. Fig.12(b), 12(c) and 12(d) are partial enlarged images of red dotted frames (1), (2) and (3) in Fig.12(a), respectively. In Fig.12(a),  $k_A$ ,  $k_B$  and  $k_C$  change 10 times from 1.3, 1 and 0.7 to 1, 0.7 and 1.3, respectively, where  $k_A$  and  $k_B$  decrease by 0.03 and  $k_C$  increases by 0.06 each time. The voltage of the adjustable voltage source in phase C increases gradually from 40V to 56V manually. Compared with the rated battery module voltage 48V in the system, the voltage changing rate is  $\pm 16.7\%$ . It can be seen from Fig.12(a) that the amplitude of  $u_{\text{out}_C1}$  is increasing continuously. In Fig.12(a), the three waveforms are synchronized, as can be seen from the waveform of  $k_C$ . The measured average values of  $k_A$ ,  $k_B$  and  $k_C$  in Fig.12(b), 12(c), 12(d) show the power generation ratios  $k_A$ ,  $k_B$  and  $k_C$  finally reach the set values of 1, 0.7 and 1.3 within the tolerance of measurement error, which also indicates that power generation ratios between phases can be well controlled. Fig.12(c) is partial enlarged images of the continuously change of power generation ratios between phases.  $k_A$ ,  $k_B$  and  $k_C$  reach the stable state after about 25ms. It is thus concluded that the MCC obtains better performance both in dynamic and steady states.

The amplified waveforms of the three-phase currents of the grid side in Fig.12(b), 12(c) and 12(d) show that the balanced three phase AC currents can still be obtained, as power generation ratios between phases and the module voltage change simultaneously. Therefore, the change of the power generation ratios between phases and the module voltage has no effect on the three phase AC currents. As can be seen from Fig.12(b) and 12(d), with the increase of module voltage, the power generation ratios between phases remains stable at the given value, indicating that the change of module voltage has no effect on the power generation ratios between phases. It also proves that the control strategy is also applicable under imbalanced module voltage conditions. In Fig.12(b), 12(c) and 12(d), the measured average value of the current  $i_{\text{dc}_C1}$  of the upper module in phase C remains unchanged. The measured average value of the battery current  $i_{\text{dc}_C2}$  of the lower module increases along with the  $k_C$ . The  $u_{\text{out}_C1}$  waveform is close to square wave, which indicates that the module of phase C is always in P or N state in each carrier cycle with the changes of  $k_C$ . Therefore, as the  $k_C$  changes, the distribution of inter-phase power can only be satisfied by adjusting the conduction time of the lower module in phase C. That is, the change of  $k_C$  is represented by the change of  $i_{\text{dc}_C2}$  in the experiment.

### 3) Inner-phase Power Control Experimental results

The inner-phase power control is the redistribution of DC power between sub-modules. An experiment on five-level inverters is carried out on the condition of  $k_A^*=k_B^*=k_C^*=1$ , to verify the suitability of the inner-phase control strategy to



voltage unbalance conditions and the continuous variability of the inner-phase power distribution. An adjustable voltage source is used as a substitute of the upper module battery of phase C in the experiment.

Fig.13(a) shows the overall waveforms of the changes of inner-phase power coefficients  $I_{A1}$ ,  $I_{B1}$  and  $I_{C1}$ , the output voltage  $u_{out\_C1}$  of upper module in phase C, the current of upper module on phase C  $i_{dc\_C1}$ , the battery current of lower module on phase C  $i_{dc\_C2}$  and three-phase currents  $i_A$ ,  $i_B$  and  $i_C$  on the power grid side. Fig.13(b), 13(c) and 13(d) are partial enlarged images of red dotted frames (1), (2) and (3) in Fig.13(a), respectively. In Fig.13(a),  $I_{A1}$ ,  $I_{B1}$  and  $I_{C1}$  changed 5 times from 1.4, 1.2 and 0.8 to 1.2, 0.8 and 1.2, respectively, where  $I_{A1}$  decreases by 0.04,  $I_{B1}$  decreases by 0.08 and  $I_{C1}$  increases by 0.08 each time. The voltage of the adjustable voltage source in phase C increases gradually from 40V to 56V manually. Compared with the rated battery module voltage 48V in the system, the voltage changing rate is  $\pm 16.7\%$ . It can be seen from Fig.13(a) that the amplitude of  $u_{out\_C1}$  is increasing continuously, indicating the continuous rising of the battery voltage. The three waveforms in Fig.13(a) are synchronized, as can be seen from the waveform of  $I_{C1}$ . The measured average values of  $I_{A1}$ ,  $I_{B1}$  and  $I_{C1}$  in Fig.13(b), 13(c), 13(d) show that inner-phase power coefficients  $I_{A1}$ ,  $I_{B1}$  and  $I_{C1}$  finally reach the set values of 1.2, 0.8 and 1.2 within the tolerance of measurement error, which also proves that the inner-phase power coefficients are well controlled. From the waveforms of  $I_{A1}$ ,  $I_{B1}$  and  $I_{C1}$  in Fig.13(c), it is thus concluded that the control strategy obtains good performance both in dynamic and steady states.

The amplified waveforms of the three-phase currents on the grid side in Fig.13 (b), 13(c) and 13(d) show that the balanced three-phase AC currents can still be obtained, as the inner-phase power coefficients and the battery voltage change simultaneously. This proves that the change of the inner-phase power coefficients and the battery voltage has no effect on the three-phase AC currents. As can be seen from Fig.13(b) and 13(d), with the increase of battery voltage, the inner-phase power coefficients remain stable at a given value. Therefore, the change of battery voltage has no effect on the inner-phase power coefficients, and it also indicates that the inner-phase power control strategy is applicable to imbalanced module voltage. In Fig.13(b), 13(c) and 13(d), the measured average value of the battery current  $i_{dc\_C2}$  of phase C changes from 2.507 to 2.024A, and finally to 1.564A. The battery voltage of the lower module in phase C remains unchanged, indicating that the battery output power of lower module in phase C decreases along with the increase of  $I_{C1}$ . However, the total output power of C-phase remains unchanged, so the output power of C-phase upper module increases, exactly conforming to the change of  $I_{C1}$ .

## VII. CONCLUSIONS

In order to improve the efficiency of PV and energy storage systems, three novel inter-phase power control methods are proposed in this paper to control the distribution of three-phase power. All the three inter-phase power control methods,

CMMM, CMPP, CMMV, can control the DC power in both low and high power systems, though with their different performances in dynamic and steady states. Based on the study of their differences, the MCC, which combines the advantages of CMPP and CMMV, is proposed to achieve optimal control of inter-phase power. The performance of MCC is proven to be as dynamic as that of CMPP, and its performance in steady state matches that of CMMV. To further improve the power control capability of CHB, the inner-phase power control method is then proposed to achieve precise power control of each submodule. Results of the simulation and experimental show that both the inter-phase and inner-phase power control methods can achieve good power control even under imbalanced voltages and can acquire balanced three-phase currents, indicating that the proposed power control methods are both practical and effective in controlling the power distribution.

## REFERENCES

- [1] J. Chavarria, D. Biel, F. Guinjoan, C. Meza and J. J. Negroni, "Energy-Balance Control of PV Cascaded Multilevel Grid-Connected Inverters Under Level-Shifted and Phase-Shifted PWMs," *IEEE Trans. Ind. Electron.*, vol. 60, no. 1, pp. 98-111, Jan. 2013.
- [2] J. Sastry, P. Bakas, H. Kim, L. Wang, and A. Marinopoulos, "Evaluation of cascaded H-bridge inverter for utility-scale photovoltaic systems," *Renew. Energy*, vol. 69, pp. 208-218, Sep. 2014.
- [3] D. Sun *et al.*, "Modeling, Impedance Design, and Efficiency Analysis of Quasi-Z Source Module in Cascaded Multilevel Photovoltaic Power System," *IEEE Trans. Ind. Electron.*, vol. 61, no. 11, pp. 6108-6117, Nov. 2014.
- [4] L. Liu, H. Li, Y. Xue and W. Liu, "Reactive Power Compensation and Optimization Strategy for Grid-Interactive Cascaded Photovoltaic Systems," *IEEE Trans. Power Electron.*, vol. 30, no. 1, pp. 188-202, Jan. 2015.
- [5] C. D. Townsend, T. J. Summers and R. E. Betz, "Phase-Shifted Carrier Modulation Techniques for Cascaded H-Bridge Multilevel Converters," *IEEE Trans. Ind. Electron.*, vol. 62, no. 11, pp. 6684-6696, Nov. 2015.
- [6] A. Marzoughi, R. Burgos, D. Boroyevich and Y. Xue, "Investigation and comparison of cascaded H-bridge and modular multilevel converter topologies for medium-voltage drive application," *IECON 2014 - 40th Annual Conference of the IEEE Industrial Electronics Society*, Dallas, TX, 2014, pp. 1562-1568.
- [7] A. Marzoughi, R. Burgos, D. Boroyevich and Y. Xue, "Design and Comparison of Cascaded H-Bridge, Modular Multilevel Converter, and 5-L Active Neutral Point Clamped Topologies for Motor Drive Applications," *IEEE Trans. Ind. Appl.*, vol. 54, no. 2, pp. 1404-1413, March-April 2018.
- [8] M. Malinowski, K. Gopakumar, J. Rodriguez and M. A. Perez, "A Survey on Cascaded Multilevel Inverters," *IEEE Trans. Ind. Electron.*, vol. 57, no. 7, pp. 2197-2206, July 2010.
- [9] Y. Yu, G. Konstantinou, B. Hredzak and V. G. Agelidis, "Operation of Cascaded H-Bridge Multilevel Converters for Large-Scale Photovoltaic Power Plants Under Bridge Failures," *IEEE Trans. Ind. Electron.*, vol. 62, no. 11, pp. 7228-7236, Nov. 2015.
- [10] Y. Yu, G. Konstantinou, B. Hredzak and V. G. Agelidis, "Optimal zero sequence injection in multilevel cascaded H-bridge converter under unbalanced photovoltaic power generation," *2014 International Power Electronics Conference (IPEC-Hiroshima 2014 - ECCE ASIA)*, Hiroshima, 2014, pp. 1458-1465.
- [11] Y. Yu, G. Konstantinou, B. Hredzak and V. G. Agelidis, "Power Balance of Cascaded H-Bridge Multilevel Converters for Large-Scale Photovoltaic Integration," *IEEE Trans. Power Electron.*, vol. 31, no. 1, pp. 292-303, Jan. 2016.
- [12] Y. Yu, G. Konstantinou, B. Hredzak and V. G. Agelidis, "Power Balance Optimization of Cascaded H-Bridge Multilevel Converters for

- Large-Scale Photovoltaic Integration," *IEEE Trans. Power Electron.*, vol. 31, no. 2, pp. 1108-1120, Feb. 2016.
- [13] Qingfeng Wu, Xiaofeng Sun, Yancong Hao, Erdong Chen and Baocheng Wang, "A SoC control strategy based on wireless droop control for energy storage systems in ac islanded microgrid," *2016 IEEE 8th International Power Electronics and Motion Control Conference (IPEMC-ECCE Asia)*, Hefei, 2016, pp. 2893-2898.
- [14] Y. Yu, G. Konstantinou, B. Hredzak and V. G. Agelidis, "On extending the energy balancing limit of multilevel cascaded H-bridge converters for large-scale photovoltaic farms," *2013 Australasian Universities Power Engineering Conference (AUPEC)*, Hobart, TAS, 2013, pp. 1-6.
- [15] B. Xiao, K. Shen, J. Mei, F. Filho and L. M. Tolbert, "Control of cascaded H-bridge multilevel inverter with individual MPPT for grid-connected photovoltaic generators," *2012 IEEE Energy Conversion Congress and Exposition (ECCE)*, Raleigh, NC, 2012, pp. 3715-3721.
- [16] S. Rivera, S. Kouro, B. Wu, J. I. Leon, J. Rodríguez and L. G. Franquelo, "Cascaded H-bridge multilevel converter multistring topology for large scale photovoltaic systems," *2011 IEEE International Symposium on Industrial Electronics*, Gdansk, 2011, pp. 1837-1844.
- [17] B. Xiao, L. Hang, J. Mei, C. Riley, L. M. Tolbert and B. Ozpineci, "Modular Cascaded H-Bridge Multilevel PV Inverter With Distributed MPPT for Grid-Connected Applications," *IEEE Trans. Ind. Appl.*, vol. 51, no. 2, pp. 1722-1731, March-April 2015.
- [18] S. Rivera, B. Wu, S. Kouro, H. Wang and D. Zhang, "Cascaded H-bridge multilevel converter topology and three-phase balance control for large scale photovoltaic systems," *2012 3rd IEEE International Symposium on Power Electronics for Distributed Generation Systems (PEDG)*, Aalborg, 2012, pp. 690-697.
- [19] R. P. Aguilera *et al.*, "Predictive Control of Cascaded H-Bridge Converters Under Unbalanced Power Generation," *IEEE Trans. Ind. Electron.*, vol. 64, no. 1, pp. 4-13, Jan. 2017.
- [20] Z. Ye *et al.*, "A Novel DC-Power Control Method for Cascaded H-Bridge Multilevel Inverter," *IEEE Trans. Ind. Electron.*, vol. 64, no. 9, pp. 6874-6884, Sept. 2017.
- [21] R. Sharma and A. Das, "Per phase power balancing in grid connected cascaded H-bridge multilevel converter for solar PV application," *2017 6th International Conference on Computer Applications in Electrical Engineering-Recent Advances (CERA)*, Roorkee, 2017, pp. 433-438.
- [22] Z. Ye *et al.*, "Simplified PWM Strategy for Neutral-Point-Clamped (NPC) Three-Level Converter," *Journal of Power Electronics*, vol. 14, no. 3, pp. 519-530, Mar. 2014.
- [23] Z. Ye, Y. Xu, X. Wu, G. Tan, X. Deng and Z. Wang, "A Simplified PWM Strategy for a Neutral-Point-Clamped (NPC) Three-Level Converter With Unbalanced DC Links," *IEEE Trans. Power Electron.*, vol. 31, no. 4, pp. 3227-3238, April 2016.



**Hanjun Pei** was born in Hubei, China, in 1996. He received his B.S. degree in electrical engineering and automation from Hubei Normal University, China, in 2018. He is currently working toward the M.S. degree in power electronics and drives in China University of Mining and Technology. His research interests include power electronics and multilevel inverter.



**Josep M. Guerrero** (S'01-M'04-SM'08-FM'15) received the B.S. degree in telecommunications engineering, the M.S. degree in electronics engineering, and the Ph.D. degree in power electronics from the Technical University of Catalonia, Barcelona, in 1997, 2000 and 2003, respectively. Since 2011, he has been a Full Professor with the Department of Energy Technology, Aalborg University, Denmark, where he is responsible for the Microgrid Research Program ([www.microgrids.et.aau.dk](http://www.microgrids.et.aau.dk)). From 2014 he is chair Professor in Shandong University; from 2015 he is a distinguished guest Professor in Hunan University; and from 2016 he is a visiting professor fellow at Aston University, UK, and a guest Professor at the Nanjing University of Posts and Telecommunications. From 2019, he became a Villum Investigator by The Villum Fonden, which supports the Center for Research on Microgrids (CROM) at Aalborg University, being Prof. Guerrero the founder and Director of the same centre.

His research interests is oriented to different microgrid aspects, including power electronics, distributed energy-storage systems, hierarchical and cooperative control, energy management systems, smart metering and the internet of things for AC/DC microgrid clusters and islanded minigrids. Specially focused on microgrid technologies applied to offshore wind and maritime microgrids for electrical ships, vessels, ferries and seaports. Prof. Guerrero is an Associate Editor for a number of IEEE TRANSACTIONS. He has published more than 500 journal papers in the fields of microgrids and renewable energy systems, which are cited more than 40,000 times. He received the best paper award of the IEEE Transactions on Energy Conversion for the period 2014-2015, and the best paper prize of IEEE-PES in 2015. As well, he received the best paper award of the Journal of Power Electronics in 2016. During six consecutive years, from 2014 to 2019, he was awarded by Clarivate Analytics (former Thomson Reuters) as Highly Cited Researcher. In 2015 he was elevated as IEEE Fellow for his contributions on "distributed power systems and microgrids."



**Zongbin Ye** (M'16) was born in Jiangxi, China, in 1983. He received the Ph.D. degree in electrical engineering from the China University of Mining and Technology, Xuzhou, China, in 2010.

Since 2015, he has been an Associate Professor in the School of Information and Electrical Engineering, China University of Mining and Technology. He has authored several journal and conference articles and also one book in the area of motor control. His research focuses on the development of high-power multilevel converters and motor drivers.



**Shiqi Mao** was born in Jiangsu, China, in 1994. He received his B.S. degree in electrical engineering and automation from Suzhou University of Science and Technology, China, in 2017. He is currently working toward the M.S. degree in power electronics and drives in China University of Mining and Technology. His research interests include power electronics and multilevel inverter.



**Qisheng Zheng** was born in Henan, China, in 1995. He received his B.S. degree in electrical engineering and automation from Henan University of Technology, China, in 2018. He is currently working toward the M.S. degree in power electronics and drives in China University of Mining and Technology. His research interests include power electronics and multilevel inverter.



**Tingting Wang** was born in Zhejiang, China, in 1994. She received the B.S. degree in electrical engineering and automation from Wuhan Textile University, Wuhan, China, in 2017. She is currently working toward the M.S. degree in power electronics and drives at the China University of Mining and Technology, Xuzhou, China. Her research interests include power electronics and multilevel inverters.



**Anni Chen** was born in Zhejiang, China, in 1993. She received the B.S. degree in electrical engineering and automation from Zhejiang University of Technology, Zhejiang, China, in 2016. She received the M.S. degree in power electronics and drives at the China University of Mining and Technology, Xuzhou, China, in 2019. She is currently working in the Zhongtian Construction Group Co., Ltd., Hangzhou, Zhejiang, China. Her research interests include power electronics and multilevel inverters.

and application of control theory to smart grids, power systems, circuits and systems, and biomedical engineering.

Prof. Fernando was an Associate Editor of the IEEE TRANSACTIONS ON INFORMATION TECHNOLOGY IN BIOMEDICINE and a Guest Editor of Optimal Control Applications and Methods. He is currently an associate editor for IEEE TCAS I and IEEE Access. And He was an associate editor for TCAS II.



**Zhiguo Zhang** was born in Shandong, China, in 1992. He received the B.S. degree in electrical engineering and automation from North-west A&F University, Xianyang, China, in 2015. He received the M.S. degree in power electronics and drives at the China University of Mining and Technology, Xuzhou, China, in 2018. He is currently working in the State Grid Yantai Power Supply Company, Yantai, Shandong, China. His research interests include power electronics and multilevel inverters.



**Linlin Jiang** was born in Anhui, China, in 1992. He received the B.S. degree in electrical engineering and automation from Anhui University of Science and Technology, Huainan, China, in 2015. He received the M.S. degree in power electronics and drives at the China University of Mining and Technology, Xuzhou, China, in 2018. He is currently working in the State Grid Jiaxing Power Supply Company, Jiaxing, Zhejiang, China. His research interests include power electronics and multilevel inverters.



**Dongsheng Yu** (M'15) received the B.Eng. and Ph.D. degrees in electrical engineering from the School of Information and Electrical Engineering, China University of Mining and Technology, Xuzhou, China, in 2005 and 2011, respectively.

He is currently an Associate Professor in the School of Information and Electrical Engineering, China University of Mining and Technology. From 2009 to 2010, he was a Visiting Student at the University of Western Australia, Crawley, Australia, where he was an Endeavour Fellow in 2014. His

research interests include power electronics, renewable energy, electric drives, nonlinear dynamics, and memristive systems. He has published one book and over 30 papers in these areas.



**Tyrone Fernando** (M'16–SM'05) received the Bachelor of Engineering (Hons.) degree in electrical engineering and the Doctor of Philosophy degree in biomedical engineering from the University of Melbourne, Melbourne, Australia, in 1990 and 1996, respectively.

In 1996, he joined the School of Electrical Electronic and Computer Engineering, University of Western Australia, Crawley, Australia, where he is currently a Professor. In 2009 and 2010, he was the Deputy Head of the School.

He has authored several journal and conference articles and also two books in the areas of functional observers and closed-loop control of blood glucose in diabetics. His research interests include estimations theory, control theory,